CRYSTAL GROWTH & DESIGN

pubs.acs.org/crystal

Article

Exploring Crystallization Phenomena in Al_2TiO_5-Based Chemical Vapor-Deposited Coatings by *in Situ* Transmission Electron Microscopy

Sebastian Öhman, Olivier Donzel-Gargand, Mats Boman, and Tobias Törndahl*

Cite This: *Cryst. Growth Des.* 2023, 23, 7680−7687

Read Online

ACCESS | Metrics & More | Article Recommendations | Supporting Information

ABSTRACT: Understanding crystallization is crucial to enable improved design approaches for inorganic materials. Despite this importance, a deepened understanding of the mechanisms controlling this phase transition is still lacking. Herein, we employ *in situ* heating in a transmission electron microscope (TEM) to unravel crystallization phenomena in an Al−Ti−O system. Specifically, annealing of amorphous chemical vapor deposited (CVD) Al_2TiO_5-based coatings has been carried out in the temperature interval 700−900 °C. Crystallization typically occurs through a two-step process, where numerous smaller (<10 nm) crystals are initially formed, followed by rapid crystal growth. Examinations of the initial crystallization stages indicate that the amorphous-to-crystalline transformation is polymorphic and that several phases may nucleate simultaneously, including $Al_6Ti_2O_{13}$ and $Al_{16}Ti_5O_{34}$. A transient (time-dependent) nucleation rate is discovered based on the displayed nucleation behavior. Subsequent evaluations of the growth stages also reveal a preferential growth into larger crystals, and the coherent findings of this study indicate that crystallization occurs through a diffusionless (displacive) mechanism.

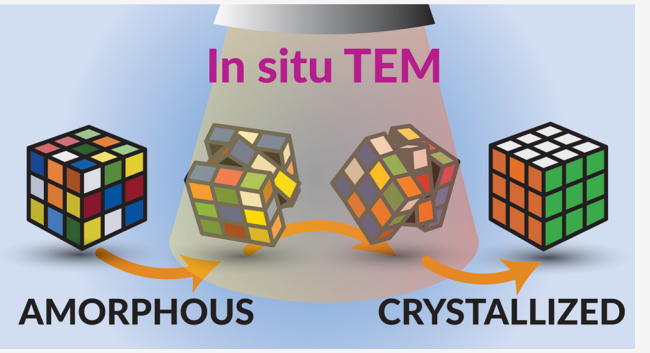

INTRODUCTION

The transition between the disordered and ordered states has tremendous importance not just in the chemistry field but also in metallurgy,[1,2] medicine,[3,4] and biology.[5,6] As such, it has attracted significant research interest since the late 19th century,[7] and its understanding has laid the foundation for the development of many ceramics,[8,9] pharmaceuticals,[10,11] phase-change memory devices,[12] and products used within information technologies.[13,14] Notwithstanding this importance, knowledge about the uttermost mechanisms controlling this transformation is still lacking. While classical nucleation theory (CNT), initially developed by Gibbs and extended by many other authors,[15−24] forms the central framework for this understanding, it also carries several limitations. Foremost, the theory does not provide any deepened explanations about the chemical interactions that may happen on the atomic scale during nucleation and growth. Such insights are increasingly demanded in pursuing functional inorganic materials through rational design approaches, particularly those that may tightly integrate thermodynamic predictions with enhanced kinetic selectivity of the syntheses.[25] Controlling the stages involved in crystallization is essential to achieve this, which may also entail improved capabilities to adjust the structure−property relationships through the evolving microstructure. Above all, controlling nucleation—the first step involved in the phase transformation—would enable improved selectivity to many metastable phases that are otherwise hard to reach by many conventional solid-state synthesis approaches.

However, understanding nucleation and growth remains challenging, mainly because of its dynamic and sometimes also unpredictable behaviors. In particular, the short time- and length scales for which nucleation occurs make it challenging to analyze by most experimental and theoretical methods.[26−29] Similarly, nucleation is frequently regarded as a stochastic event capable of scaling several orders of magnitude in both time and geometrical dimensions, not least during the subsequent growth stages. Thus, extensive spatial resolution is required to capture these events thoroughly.[30,31] In addition, while crystallization is a dynamic process, most analyses are carried out *ex situ*, where the lack of temporal acquisition capabilities makes it difficult, if not impossible, to arrange observations into a proper time frame correctly.[25] The latter statement is especially true when competing or parallel

Received: March 31, 2023
Revised: September 22, 2023
Published: October 10, 2023

https://doi.org/10.1021/acs.cgd.3c00395
Cryst. Growth Des. 2023, 23, 7680−7687

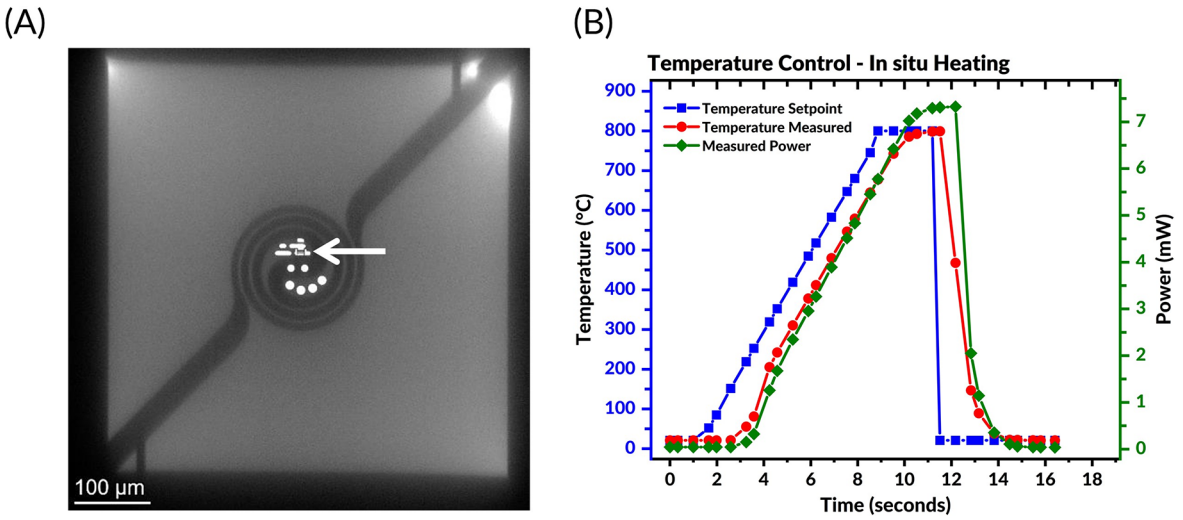

Figure 1. (A) Overview of *in situ* heating setup in the TEM. One can observe the metallic heating spiral on the silicon nitride membrane. The lamella can be placed at the center at one of the openings. The arrow points to the actual lamella. (B) Check of temperature control for the used heating stage. The heating and cooling rates are approximately 100 °C/s and −500 °C/s, respectively.

processes may occur. Accordingly, few techniques allow one to gain a comprehensive and deepened image of the steps involved during crystallization.

Nonetheless, the continuous development of analytical *in situ* techniques has provided unprecedented capabilities to study chemical phenomena as they happen, when they happen. Among these, the emergence of *in situ* transmission electron microscopy (TEM) has allowed vastly improved mechanistic insights to be made about many chemical processes, including crystallization.[32,33]

In light of this, this study aims to bring a new fundamental understanding of the nucleation and growth processes in the Al−Ti−O system by employing *in situ* heating in a TEM. Herein, we focus on crystallizing Al_2TiO_5-based chemically vapor-deposited (CVD) coatings, a material renowned for its low-to-negative thermal expansion.[34,35] The findings of this study illustrate a diminishing role of diffusion during crystallization, thereby also highlighting nucleation's role in controlling the entire crystallization event.

METHODS

As-deposited (amorphous) Al_2TiO_5-based coatings were prepared on p-type Si (100) substrates using an in-house built CVD instrument. Titanium- (TIP) and aluminum isopropoxides (AIP) were simultaneously used as precursors during the depositions, which were made at 450 °C for 1 h. Detailed experimental and technical descriptions of the CVD process can be found elsewhere.[36] The Al/Ti ratio of the coating, determined in our previous studies using energy-dispersive X-ray spectroscopy (EDS) and Rutherford backscattering spectrometry (RBS),[37] was 1.93(1), i.e., close to the ∼ ideal 2:1 ratio.

The TEM lamellae were prepared using a focused ion beam (FIB) Crossbeam 550 (Zeiss) and cut vertically from the top surface downward, following the thin film's deposition direction. To protect the thin film and limit the drift during the preparation, the sample was coated *ex situ* with a layer of carbon followed by 30 nm of Au/Pd, then *in situ* with Pt. All the FIB lamellae were lifted-out using an Omniprobe 200 (Oxford instruments) and soldered directly on the heating chips (Wildfire, DENSsolution). As shown in Figure 1A, the lamellae were positioned in the vicinity of the heating coil center, where the temperature is expected to be the most uniform.[38]

The ion polishing of the lamellae was performed on the chip itself, and the ion beam damages were minimized by applying a final polishing at 2 kV on both sides. The temperature calibration corresponding to each chip was carefully set before starting each experiment.

A Titan Themis 200 (Thermofisher, formerly FEI) was used for the transmission electron microscopy analyses. *In situ* heating experiments were achieved employing the Wildfire setup (DENSsolution). The chemical composition was measured with a SuperX energy dispersive X-ray detector (EDS, Oxford instruments), and the data were evaluated using the HyperSpy Python package.[39] The selected area electron diffraction (SAED) patterns were analyzed using CrysTBox software.[40] In total, five lamellae were prepared for analyses, whose experimental details are outlined in Table 1. The used heating temperatures varied between 700−900 °C during the *in situ* examinations, depending on the chip.

Table 1. Summary of Performed Analyses and the Main Crystallization Features Observed

chip designation	sample preparation	examined T range (° C)	heating times
1.	Ok	700−800	108 min
2.	Surface Precipitates	750−800	31 min
		800−900	14 min
3.	Good	750	60 min
		900	<300 ms
4.	Good	800	6.5 min
		800	4 min
5.	Good	800	5 min
		780−900	9 min

Irradiation from the electron beam is an intrinsic part of any TEM investigation, which may induce radiation effects in solid materials. These include, for example, (1) ionization (i.e., radiolysis), (2) electron-beam heating, and (3) knock-on atomic displacements.[41] In particular, exposures to ionizing radiation may lead to the migration and annihilation of defects that may either retard or promote structural transitions, including crystallization and nanocrystal formations.[42] Furthermore, depending on the sample's thermal conductivity, irradiations from the electron beam may also lead to a heat increase due to an accumulation of phonons.[41] In terms of crystallization, we note that even after prolonged irradiations of the samples at high temperatures (but below the main crystallization onset temperatures for Al_2TiO_5, $Al_6Ti_2O_{13}$, and $Al_{16}Ti_5O_{34}$), all samples remained amorphous, and no visible alterations could be observed. Likewise, the temperatures where crystallization of these

https://doi.org/10.1021/acs.cgd.3c00395
Cryst. Growth Des. 2023, 23, 7680−7687

phases readily occurs upon heating conform with our previous investigations.[36,43,44] For these reasons, the potential contribution from the electron beam on the overall crystallization behavior can be deemed small compared to the overall effect of the annealing temperature.

Because of the low thermal inertia of the TEM lamellae, the possible heating rates can be swift (i.e., about 100 °C/s), which is outlined in Figure 1B. Similarly, as soon as the heating is turned off, rapid cooling of the lamella occurs (about −500 °C/s). Therefore, the crystallization process can be "frozen" in its present condition, allowing its features to be studied at room temperature.

When changing the annealing temperature, the focus was adjusted to compensate for the evolving bulge of the silicon nitride membrane. However, no other alterations, such as extensive thermal drifting, were observed during the measurements.

RESULTS AND DISCUSSION

Figure 2A is a bright-field (BF) image showing an ion-polished cross-sectional lamella of an as-deposited $Al_xTi_yO_z$ coating

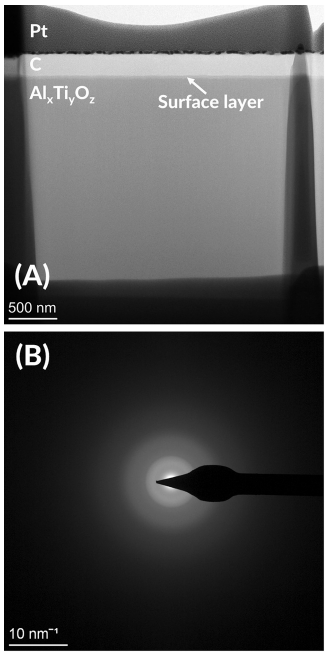

Figure 2. (A) Bright-field TEM image of a cross-section for the $Al_xTi_yO_z$ coating and (B) the corresponding electron diffraction pattern, confirming that the as-deposited coating is amorphous.

before starting the *in situ* annealing. The thin film appears amorphous, which is also supported by selected area electron diffraction (SAED, Figure 2B). The surface layer at the top of the thin film is Al-enriched and originates from the deposition process, where AIP resides for a slightly longer time in the deposition chamber at the end of the coating process.

Initial annealing experiments (Chips 1 and 2) revealed that the coatings crystallized with reasonable speed in the examined temperature interval of 800−900 °C. For example, at 800 °C, numerous smaller crystals started to appear after about 5−8 min of isothermal annealing. These crystals nucleated mainly in the upper half of the lamella with different sizes and shapes, as illustrated in Figure 3B.

In order to examine the growth behavior and subsequent stages of crystallization, the isothermal annealing was resumed. In the case of Chip 3−4−5, numerous smaller crystals continued to nucleate within the amorphous matrix upon

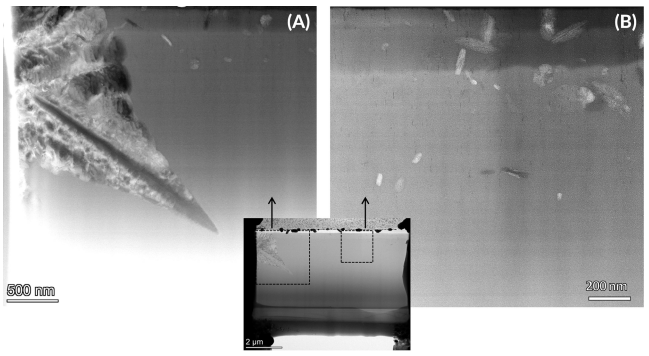

Figure 3. Bright-field TEM overview images of initially formed crystals in the lamella of Chip 5, seen as a large needle-like crystal in (A) and numerous smaller crystals within the amorphous matrix in (B). Black rectangles mark where the images in (A) and (B) are taken.

further annealing. As a general note, the growth of these initially emerged crystals occurred very slowly. On the contrary, a rapid and anisotropic crystal growth is noticed at the finalizing stages of the crystallization process, as shown in Figure 3A. Particularly, after a few minutes of additional annealing, a crystalline phase wave suddenly emerges from the side of the lamella, rapidly sweeping through the amorphous matrix at various speeds in different directions. As seen from Chip 4 and Figure S1 in the Supporting Information, the phase wave envelops any preformed crystals without any apparent alterations to their general appearances or sizes.

The fact that crystals emanate within the amorphous matrix (cf. Figure 3) suggests that they may nucleate through a homogeneous mechanism; however, one cannot exclude the possibility that these features arise at the surface of the lamella. Irrespectively, previous kinetic evaluations using the Avrami equation have indicated a homogeneous nucleation process when the Al/Ti ratio of the coating is close to 2:1.[37]

To evaluate any possible changes in chemical composition during the crystallization process, high-angle annular dark field imaging in scanning mode (STEM-HAADF) was used together with EDS. These results are compiled in Figure 4.

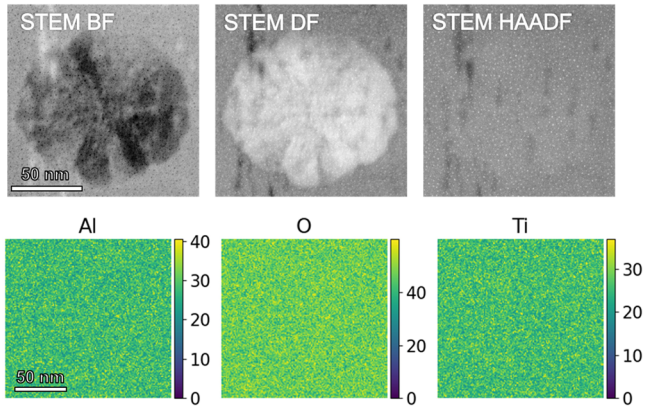

Figure 4. (Top) STEM dark-field and bright-field images coupled with STEM HAADF. Images are taken at room temperature after annealing at 800 °C for 7 min from Chip 4 (cf. Table 1). The white "dots" that are seen in the images are tiny precipitates at the surface of the lamella, which appear in the first minutes of heating in the TEM. (Bottom) EDS chemical composition maps (atom % relative) around the crystal. No compositional difference or gradient between the amorphous and crystalline regions can be detected.

https://doi.org/10.1021/acs.cgd.3c00395
Cryst. Growth Des. 2023, 23, 7680−7687

While clear diffraction contrast can be noticed by the dark-field (DF) and bright-field (BF) images, the STEM-HAADF image shows no substantial contrast between the crystalline and amorphous regions. This indicates that these two regions comprise a similar average atomic weight and that no significant phase separation occurs as part of the crystallization event. The EDS maps corroborate these findings, showing no compositional variation between the crystalline and amorphous regions. Consequently, these results indicate that the phase transformations are predominantly polymorphic (i.e., without compositional changes), which is also coherent with our previous examinations using *in situ* Rutherford backscattering spectrometry.[44]

Based on the initial nucleation behavior in Chip 4, it is possible to estimate a nucleation rate (I_t) from manual counting of the emerging crystal population N as a function of time, i.e. $I_t = \frac{dN}{dt}$. This is compiled in Figure 5A, showing an

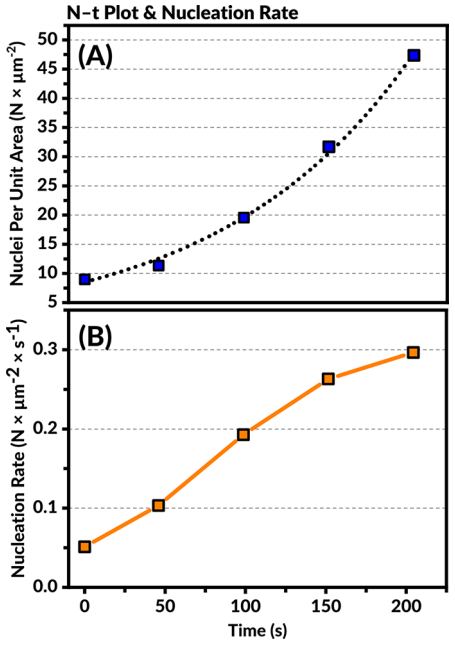

Figure 5. (A) $N-t$ plot demonstrating the evolution of the nucleation population with time. A transient (time-dependent) nucleation behavior is observed. An exponential trend is emphasized by the black dotted line. (B) Progression of the nucleation rate with time.

exponentially increasing crystal population density characteristic of a time-dependent (transient) nucleation behavior. The nucleation rate increases until the crystallization front converts the remaining amorphous bulk, incorporating any preforming crystals.

Knowing that the nucleation rate eventually reaches its uppermost (steady-state) value, the nucleation rate can be approximated from the first derivative of the curve (Figure 5B). The highest calculated value, representing the stages before the nucleation rate decreases as part of the crystal phase wave progression, was 0.3 N × μm^{-2} × s^{-1}.

A new experiment (Chip 5) was set up to further understand the crystal front wave's progression and its corresponding growth behavior; see Figure 6. Similar to Chip 4, initial crystals were observed after around 5 min, after which a crystal front wave appeared from the side of the lamella. Notably, the growth of the crystal front also occurred anisotropically, growing in the form of needle-like extensions (cf. Figure 3A). Due to the rapid growth of the crystal front wave at elevated annealing temperatures, it was not possible to follow the crystallization events in real-time with, for example, detailed diffraction analyses. However, in the middle of the crystal front wave's progression, the heating was switched off, and the rapid cooling of the lamella (cf. Figure 1) allowed us to freeze the current state of the crystallization front to study its features back at room temperature.

Based on the image series and the expansion of the crystal front wave, an upper phase-boundary velocity (v_{pb}) can be given, having units of distance per time.[45] This is shown in Figure 7, where the lateral expansion of the crystal front follows a linear relationship with a constant phase-boundary velocity of 0.052(1) $\mu m \times s^{-1}$.

The rapid progression of the crystal front wave, along with the relatively slow nucleation rate, emphasizes the role of nucleation (rather than diffusion) during the crystallization event. Notably, our previous kinetic evaluations have indicated a nucleation-controlled crystallization process in cases where the overall stoichiometry of the coating is close-to-ideal with respect to the main Al_2TiO_5 phase.[37] A characteristic feature of a nucleation-controlled process is a strong temperature dependency on the transformation rate.[46] Interestingly, such strong temperature dependency can be observed from the peculiar transformation of Chip 3, given by an image series in the Supporting Information, Figure S2.

As seen from this supporting figure, after an initial annealing period of approximately 1 h at 750 °C, the isothermal annealing temperature was raised to 900 °C. At this temperature, the rapid growth of the crystalline phase occurs until the entire amorphous matrix suddenly collapses and crystallizes virtually instantaneously (i.e., in one image frame, which is less than 300 ms). In actuality, the duration of the crystallization process is much shorter than that since the frame rate was too low to capture the complete transformation. Note that a slight radial blur also occurs in the image series due to a change in magnification during the transformation.

Similar to the crystal front wave progression in Chip 5, the rapid transformation in Chip 3 not only indicates a nucleation-controlled crystallization process where the typical slow crystal growth by diffusion is not the rate-limiting step. Because structural relaxations are a much faster process than any growth by diffusion,[47] it also indicates that the transformation does not require any substantial diffusion to occur in the first place. Thus, it demonstrates that the coatings undergo a diffusionless (displacive) amorphous-to-crystalline transformation, in coherence with our previous results and findings.[44]

Besides the rapid growth of the crystal front wave, its anisotropic growth behavior is also interesting to note. Seen particularly for Chip 5 on further annealing at 800 °C, the growth rate diminishes and eventually stops close to the substrate until the temperature increases to higher values. Following the rise, the growth continues until it is stopped again, leaving a bed of untransformed amorphous material close to the underlying silicon substrate. The untransformed layer was examined using EDS mapping (Figure 6, right), which shows that the layer is Al-enriched and contains a compositional gradient in the CVD-growth direction. An EDS profile acquired in a SEM from a cleaved sample (without any beam exposure) can also be found in the Supporting Information, Figure S6.

https://doi.org/10.1021/acs.cgd.3c00395
Cryst. Growth Des. 2023, 23, 7680−7687

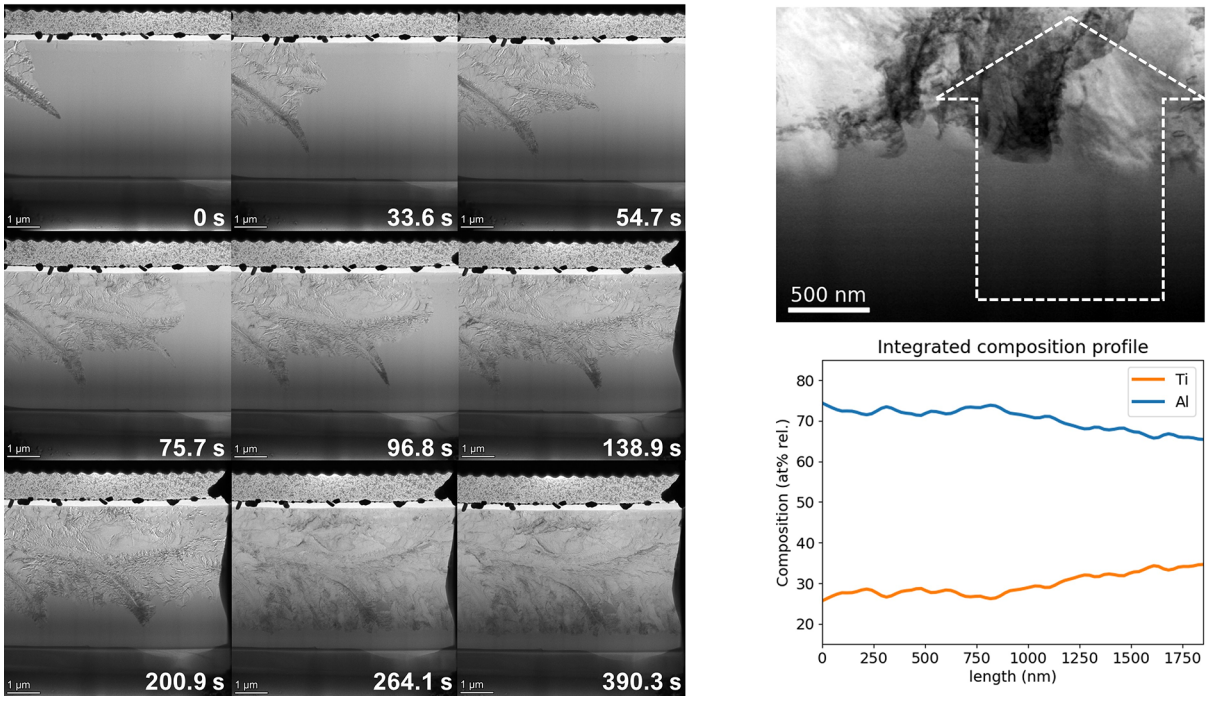

Figure 6. (Left) Image series from isothermal annealing of Chip 5 at 800 °C, displaying the progression of the crystal wave with time. (Right) Bright-field overview image of the untransformed layer close to the silicon substrate, along with an integrated composition profile starting from the bottom toward the front interface (as marked by the white arrow). Compositional values derived from EDS analysis, showing the presence of a compositional gradient in the untransformed layer.

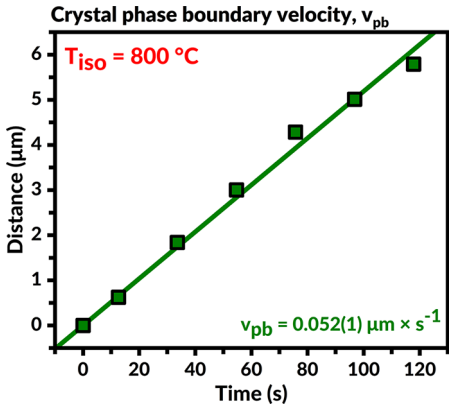

Figure 7. Calculation of the linear phase boundary velocity (v_{pb}) for the progression of the crystal front wave in Chip 5.

The compositional gradient and slow growth near the substrate suggest that crystallization are impeded in Al-enriched environments. it also indicates that nucleation and subsequent growth occur more preferably as the Ti-content in the coating increases. Accordingly, these notions highlight the potential elemental influence of titanium in the crystallization process, which agrees with our previous examinations.[37]

Interestingly, the potential elemental influence of titanium has previously been examined in the literature regarding the Al_2TiO_5 phase. For example, while Al_2TiO_5, in particular, has been shown to display cationic disordering, Norberg et al. demonstrated that a slight site preference exists for titanium in the M1 (4c) site of this phase.[48,49] In that regard, Skala et al. have also demonstrated that significant bond reconstructions that mainly occur to the M1 site in Al_2TiO_5 occur upon increasing temperature.[34] Thus, these earlier results, along with our newer ones, support the perception that titanium, as an element, likely plays an essential part in the crystallization of Al_2TiO_5, and possibly $Al_6Ti_2O_{13}$ and $Al_{16}Ti_5O_{34}$ as well.

Electron diffraction was used to analyze the crystalline phase content, where diffraction patterns of some emerged crystals in Chip 4 are shown in Figure 8a–f. Distinct electron diffraction

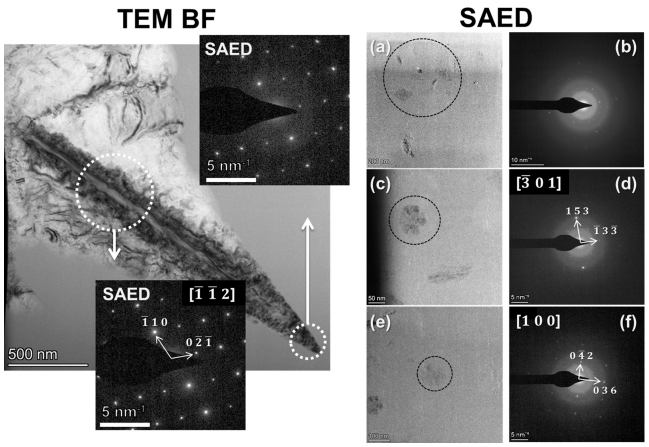

Figure 8. (Left) Interrupted crystallization process from Chip 5, showing a TEM BF image of the fast-growing needle-like crystal and its associated electron diffraction patterns. The white dashed circles indicate the locations of the patterns. (Right) Evaluation of initially emerged crystals in the amorphous matrix from the topmost half of the lamella in Chip 4, seen by an overview in (a) and the corresponding electron diffraction in (b). Closer inspections of some crystals are given in (c) and (e), and their two distinct electron diffraction patterns can be viewed in (d) and (f). The white stripes seen in the images are present before heating. All images and analyses were performed at room temperature after annealing at 800 °C.

https://doi.org/10.1021/acs.cgd.3c00395
Cryst. Growth Des. 2023, 23, 7680−7687

patterns are seen for the crystallites formed in the amorphous matrix. Here, the SAED for the overview in (b) shows a complicated pattern related to several different crystallites. Further measurements of individual crystals in (d) and (f) indicate that the probed crystals correspond to either different crystalline phases or a single phase with different lattice orientations. In order to evaluate this, indexing of the emerged patterns was made, whose results can be found in the Supporting Information, Figures S3−S4. The goodness of the fittings shows that the observed patterns can be indexed to the phases Al_2TiO_5, $Al_6Ti_2O_{13}$, and $Al_{16}Ti_5O_{34}$, which implies that more than one phase may nucleate as part of the crystallization process. Notably, this conforms to our previous studies using *in situ* X-ray diffraction[37] and Raman spectroscopy,[36] which illustrates that no other phases (like binary Al_2O_3 or TiO_2) seem to nucleate when the Al/Ti content of the films are either close-to-ideal or Al-enriched with respect to the Al_2TiO_5 phase. However, in regards to electron diffraction, it must be noted that it is possible to index Al_2TiO_5, $Al_6Ti_2O_{13}$, and $Al_{16}Ti_5O_{34}$ interchangeably to the emerged patterns, which is likely because the phases are very structurally similar. For instance, in the structural models of $Al_6Ti_2O_{13}$ and $Al_{16}Ti_5O_{34}$, the phases share almost the same structural features as Al_2TiO_5, with similar *a*- and *b*-axes but with significant extensions of their *c*-axes.[48−51] These extensions are, in turn, caused by the presence of lower coordinating sites.[50,51] For that reason, separating these phases from each other by merely considering the emerged electron diffraction patterns remains challenging, as it likely depends on the imaged zone axis.

As noticed from SAED, the tip and core of the needle-like crystal domain in Chip 5 (Figure 8, Left) are actually the same crystal, as confirmed by the identical electron diffraction patterns and the indexing of these (see Figure S5 of the Supporting Information). This supports that the crystal front wave predominantly grows and propagates into larger crystals. However, in that regard, it is recalled that no easy separation between the Al_2TiO_5, $Al_6Ti_2O_{13}$, and $Al_{16}Ti_5O_{34}$ phases can be made by fitting these diffraction patterns.

In the HRTEM image of Figure 9, a sharp interface between the amorphous and crystalline regions can be seen. Additionally, similar to the results in Figure 4 (Top), a STEM-HAADF overview image of the crystalline region (Figure S7, see Supporting Information) demonstrates an insignificant contrast deviation between the amorphous and crystalline regions. Consequently, these observations suggest that only small structural reorganizations are involved in the amorphous-to-crystalline transformation, in other words, a transformation requiring limited diffusion to occur. This notion is consistent with our previous findings combining *in situ* heating hard X-ray photoelectron spectroscopy (HAXPES) and theoretical calculations, showing that structural relaxations of oxygen are predominantly involved in the crystallization process.[44]

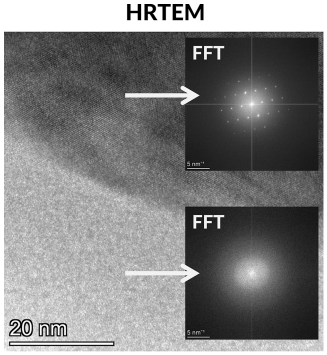

Figure 9. HRTEM image of the needle-like crystal from Chip 5, with corresponding fast-Fourier transform images in the crystalline region and the immediate surrounding. A sharp transition between crystalline and amorphous regions can be seen.

The possibilities of a displacive (i.e., diffusionless) transformation can be rationalized based on a strong structural homology between the amorphous and crystalline states of Al_2TiO_5, $Al_6Ti_2O_{13}$, and $Al_{16}Ti_5O_{34}$. To exemplify, our previous examinations by Raman spectroscopy have shown that an extensive short-range ordering of heterometallic Al−O−Ti bond assemblages exists in the amorphous as-deposited coatings.[36] In addition, Al_2TiO_5, $Al_6Ti_2O_{13}$, and $Al_{16}Ti_5O_{34}$ are structurally similar, both on the short-range and long-range ordering,[49−51] and these phases also display cationic disordering in their crystalline states.[34,35,52,53] In other words, few crystallographic restrictions are imposed on these phases. In such conditions, the difference in configurational entropy (S_{config}) between the amorphous and crystalline states becomes small,[47] implying that only short-range bond reconstructions (relaxations) should predominantly be required for the transformation to occur. The rapid progression of the phase wave seen in Chip 5 supports this perception, as demonstrated by the image series in Figure 6. Therefore, this study highlights a situation where nucleation, rather than diffusion, controls the crystallization process.

SUMMARY AND CONCLUSIONS

The crystallization of Al_2TiO_5-based CVD coatings has been examined using *in situ* heating in a transmission electron microscope. Measurements were conducted on five lamellae from the same sample, yielding similar results. Coatings readily crystallize above 800 °C by illustrating the initial formation of several nanometer-sized crystals, followed by growth from a rapidly expanding and propagating phase wave. Evaluations of the initially formed crystals by selected area diffraction show that the emerged diffraction patterns can be interchangeably indexed to the phases Al_2TiO_5, $Al_6Ti_2O_{13}$, and $Al_{16}Ti_5O_{34}$. This indicates that more than one phase may nucleate as part of the crystallization event.

Further examinations of the emerged crystallites by STEM-HAADF and EDS corroborate that no chemical fluctuations or phase separations occur as part of the crystallization event. Thus, the amorphous-to-crystalline transformation appears to be entirely polymorphic.

The continuous expansion and growth of the phase wave were also examined. Figure 6 shows that growth occurs anisotropically in seemingly preferred directions and slows down dramatically toward the rear interface, leaving a small bed of untransformed coating at the bottom close to the underlying silicon substrate. Further inspections by EDS revealed that this layer was Al-enriched and that a vertical compositional gradient existed in this layer. Coupled with previous kinetic examinations and a literature survey, these findings highlight titanium's specific involvement in the crystallization process of the Al_2TiO_5-based coatings.

An estimated nucleation rate (I_t) was extracted for one of the examined crystallization processes. The highest value was calculated to be 0.3 $N \times \mu m^{-2} \times s^{-1}$, and the exponential trend in nuclei population with time indicates a transient (time-dependent) nucleation behavior.

https://doi.org/10.1021/acs.cgd.3c00395
Cryst. Growth Des. 2023, 23, 7680−7687

The rapid heating and cooling capabilities of the *in situ* heating setup allowed us to freeze the growth of the crystallization wave to study its features at room temperature. Interestingly, the core and front of the formed crystalline domain exhibited identical electron diffraction patterns; thus, these findings support that the crystal front wave grows into larger crystals.

High-resolution imaging of the crystal−amorphous interface showed a sharp transition to the amorphous region. Combined with HAADF-imaging, yielding insignificant contrast differences, the observations indicate that the amorphous-to-crystalline transformation occurs through a diffusionless (displacive) mechanism. This perception is also strengthened by the rapid crystallization of the lamellas, particularly when the annealing temperature is further increased. Overall, these behaviors highlight a situation where nucleation—rather than growth by diffusion—controls the crystallization process.

■ ASSOCIATED CONTENT

Supporting Information

The Supporting Information is available free of charge at https://pubs.acs.org/doi/10.1021/acs.cgd.3c00395.

Image series of crystallization progression from Chips 3 and 4, SAED patterns and corresponding indexing for Chips 4 and 5, EDS compositional profile of a cleaved sample, STEM-HAADF overview for the interrupted crystallization process in Chip 5 (PDF)

■ AUTHOR INFORMATION

Corresponding Author

Tobias Törndahl − *Department of Materials Science and Engineering, Solar Cell Technology, Ångström Laboratory, Uppsala University, Uppsala SE-75103, Sweden;* orcid.org/0000-0001-7757-5847; Email: Tobias.Torndahl@angstrom.uu.se

Authors

Sebastian Öhman − *Inorganic Chemistry, Department of Chemistry, Ångström Laboratory, Uppsala University, Uppsala SE-75121, Sweden;* orcid.org/0000-0002-7071-3917

Olivier Donzel-Gargand − *Department of Materials Science and Engineering, Solar Cell Technology, Ångström Laboratory, Uppsala University, Uppsala SE-75103, Sweden;* orcid.org/0000-0002-2101-3746

Mats Boman − *Inorganic Chemistry, Department of Chemistry, Ångström Laboratory, Uppsala University, Uppsala SE-75121, Sweden;* orcid.org/0000-0002-7018-9617

Complete contact information is available at: https://pubs.acs.org/10.1021/acs.cgd.3c00395

Notes

The authors declare no competing financial interest.

■ ACKNOWLEDGMENTS

The Swedish Foundation for Strategic Research (SSF), contract RMA15-0048, is acknowledged for its financial support. Further support for TEM operation from the Department of Materials Science and Engineering, Uppsala University, is also acknowledged. The authors also acknowledge Myfab Uppsala for providing facilities and experimental support for the TEM instrument. Myfab is funded by the Swedish Research Council (2019-00207) as a national research infrastructure.

■ REFERENCES

(1) Greer, A. L. Crystallization of Amorphous Alloys. *Metall. Mater. Trans. A* **1996**, *27* (3), 549−555.

(2) Sohrabi, N.; Jhabvala, J.; Logé, R. E. Additive Manufacturing of Bulk Metallic Glasses—Process, Challenges and Properties: A Review. *Metals (Basel).* **2021**, *11* (8), 1279.

(3) Tosheva, L.; Valtchev, V. P. Nanozeolites: Synthesis, Crystallization Mechanism, and Applications. *Chem. Mater.* **2005**, *17* (10), 2494−2513.

(4) Taylor, L. S.; Braun, D. E.; Steed, J. W. Crystals and Crystallization in Drug Delivery Design. *Cryst. Growth Des.* **2021**, *21* (3), 1375−1377.

(5) Stevens, R. C. High-Throughput Protein Crystallization. *Curr. Opin. Struct. Biol.* **2000**, *10* (5), 558−563.

(6) Vekilov, P. G.; Vorontsova, M. A. Nucleation Precursors in Protein Crystallization. *Acta Crystallogr. Sect. F Struct. Biol. Commun.* **2014**, *70* (3), 271−282.

(7) Gibbs, J. W. On the Equilibrium of Heterogeneous Substances. *Trans. Connect. Acad. Arts Sci.* **1876**, *3*, 108−248 343−524.

(8) Höland, W.; Rheinberger, V.; Schweiger, M. Control of Nucleation in Glass Ceramics. *Philos. Trans. R. Soc. London. Ser. A Math. Phys. Eng. Sci.* **2003**, *361* (1804), 575−589.

(9) Liu, H.; Jiang, Q.; Huo, J.; Zhang, Y.; Yang, W.; Li, X. Crystallization in Additive Manufacturing of Metallic Glasses: A Review. *Addit. Manuf.* **2020**, *36* (March), 101568.

(10) Gao, Z.; Rohani, S.; Gong, J.; Wang, J. Recent Developments in the Crystallization Process: Toward the Pharmaceutical Industry. *Engineering* **2017**, *3* (3), 343−353.

(11) Orehek, J.; Teslić, D.; Likozar, B. Continuous Crystallization Processes in Pharmaceutical Manufacturing: A Review. *Org. Process Res. Dev.* **2021**, *25* (1), 16−42.

(12) Raoux, S.; Xiong, F.; Wuttig, M.; Pop, E. Phase Change Materials and Phase Change Memory. *MRS Bull.* **2014**, *39* (8), 703−710.

(13) Patra, P.; Annapurna, K. Transparent Tellurite Glass-Ceramics for Photonics Applications: A Comprehensive Review on Crystalline Phases and Crystallization Mechanisms. *Prog. Mater. Sci.* **2022**, *125*, 100890.

(14) Komatsu, T. Design and Control of Crystallization in Oxide Glasses. *J. Non. Cryst. Solids* **2015**, *428*, 156−175.

(15) Volmer, M.; Weber, A. Z. Nucleus Formation in Supersaturated Systems. *Z. Phys. Chem.* **1926**, *119*, 277−301.

(16) Farkas, L. Keimbildungsgeschwindigkeit in Übersättigten Dämpfen. *Z. Phys. Chem.***1927**, *125U* (1), 236−242..

(17) Becker, R.; Döring, W. Kinetische Behandlung Der Keimbildung in Übersättigten Dämpfen. *Ann. Phys.* **1935**, *416* (8), 719−752.

(18) Fisher, J. C.; Hollomon, J. H.; Turnbull, D. Nucleation. *J. Appl. Phys.* **1948**, *19* (8), 775−784.

(19) Turnbull, D.; Fisher, J. C. Rate of Nucleation in Condensed Systems. *J. Chem. Phys.* **1949**, *17* (1), 71−73.

(20) Kolmogorov, A. N. Vol. II: Probability Theory and Mathematical Statistics. In *Selected Works of A. N. Kolmogorov*; Shiryaev, A. N.; Lindquist, G., Eds.; Springer International Publishing, Dordrecht, 1992; pp 188−192, DOI: 10.1007/978-94-011-2260-3.

(21) Johnson, W. A.; Mehl, R. F. Reaction Kinetics in Processes of Nucleation and Growth. *Trans. Am. Inst. Min. Metall. Eng.* **1939**, *135*, 416−442.

(22) Avrami, M. Kinetics of Phase Change. I: General Theory. *J. Chem. Phys.* **1939**, *7* (12), 1103−1112.

(23) Avrami, M. Kinetics of Phase Change. II Transformation-Time Relations for Random Distribution of Nuclei. *J. Chem. Phys.* **1940**, *8* (2), 212−224.

(24) Avrami, M. Granulation, Phase Change, and Microstructure Kinetics of Phase Change. III. *J. Chem. Phys.* **1941**, *9* (2), 177−184.
(25) Sutter-Fella, C. M. The Value of Watching How Materials Grow: A Multimodal Case Study on Halide Perovskites. *Adv. Energy Mater.* **2021**, *11* (17), 2003534.
(26) De Yoreo, J. J. In-Situ Liquid Phase TEM Observations of Nucleation and Growth Processes. *Prog. Cryst. Growth Charact. Mater.* **2016**, *62* (2), 69−88.
(27) Nielsen, M. H.; Aloni, S.; De Yoreo, J. J. In Situ TEM Imaging of $CaCO_3$ Nucleation Reveals Coexistence of Direct and Indirect Pathways. *Science (80-.).* **2014**, *345* (6201), 1158−1162.
(28) Karthika, S.; Radhakrishnan, T. K.; Kalaichelvi, P. A Review of Classical and Nonclassical Nucleation Theories. *Cryst. Growth Des.* **2016**, *16* (11), 6663−6681.
(29) Lodesani, F.; Tavanti, F.; Menziani, M. C.; Maeda, K.; Takato, Y.; Urata, S.; Pedone, A. Exploring the Crystallization Path of Lithium Disilicate through Metadynamics Simulations. *Phys. Rev. Mater.* **2021**, *5* (7), 075602.
(30) Dey, A.; de With, G.; Sommerdijk, N. A. J. M. In Situ Techniques in Biomimetic Mineralization Studies of Calcium Carbonate. *Chem. Soc. Rev.* **2010**, *39* (2), 397−409.
(31) Smeets, P. J. M.; Cho, K. R.; Kempen, R. G. E.; Sommerdijk, N. A. J. M.; De Yoreo, J. J. Calcium Carbonate Nucleation Driven by Ion Binding in a Biomimetic Matrix Revealed by in Situ Electron Microscopy. *Nat. Mater.* **2015**, *14* (4), 394−399.
(32) Hayzelden, C.; Batstone, J. L.; Cammarata, R. C. In Situ Transmission Electron Microscopy Studies of Silicide-Mediated Crystallization of Amorphous Silicon. *Appl. Phys. Lett.* **1992**, *60* (2), 225−227.
(33) Pienack, N.; Bensch, W. In-Situ Monitoring of the Formation of Crystalline Solids. *Angew. Chemie Int. Ed.* **2011**, *50* (9), 2014−2034.
(34) Skala, R. D.; Li, D.; Low, I. M. Diffraction, Structure and Phase Stability Studies on Aluminium Titanate. *J. Eur. Ceram. Soc.* **2009**, *29* (1), 67−75.
(35) Morosin, B.; Lynch, R. W. Structure Studies on Al2TiO5 at Room Temperature and at 600°C. *Acta Crystallogr. Sect. B Struct. Crystallogr. Cryst. Chem.* **1972**, *28* (4), 1040−1046.
(36) Öhman, S.; Qiu, R.; Edvinsson, T.; Bäcke, O.; Törndahl, T.; Boman, M. Selective Kinetic Growth and Role of Local Coordination in Forming Al_2TiO_5-Based Coatings at Lower Temperatures. *Mater. Adv.* **2021**, *2* (17), 5737−5751.
(37) Öhman, S.; Ek, G.; Nagy, G.; Törndahl, T.; Primetzhofer, D.; Boman, M. Circumventing Thermodynamic Constraints in Nucleation-Controlled Crystallization of Al2TiO5-Based Chemical Vapor Deposition Coatings. *Chem. Mater.* **2022**, *34* (11), 5151−5164.
(38) van Omme, J. T.; Zakhozheva, M.; Spruit, R. G.; Sholkina, M.; Pérez Garza, H. H. Advanced Microheater for in Situ Transmission Electron Microscopy; Enabling Unexplored Analytical Studies and Extreme Spatial Stability. *Ultramicroscopy* **2018**, *192*, 14−20.
(39) de la Peña, F.; Prestat, E.; Fauske, V. T.; Burdet, P.; Lähnemann, J.; Jokubauskas, P.; Furnival, T.; Nord, M.; Ostasevicius, T.; MacArthur, K. E.; Johnstone, D. N.; Sarahan, M.; Taillon, J.; Aarholt, T.; Migunov, V.; Eljarrat, A.; Caron, J.; Francis, C.; Nemoto, T.; Poon, T.; Mazzucco, S.; Tappy, N.; Cautaerts, N.; Somnath, S.; Slater, T.; Walls, M.; Winkler, F.; Ånes, H. W. *Hyperspy/Hyperspy*; Release v1.7.3, 2022, DOI: 10.5281/zenodo.592838.
(40) Klinger, M. More Features, More Tools, More CrysTBox. *J. Appl. Crystallogr.* **2017**, *50* (4), 1226−1234.
(41) Chung, T. F.; Yang, Y. L.; Huang, B. M.; Shi, Z.; Lin, J.; Ohmura, T.; Yang, J. R. Transmission Electron Microscopy Investigation of Separated Nucleation and In-Situ Nucleation in AA7050 Aluminium Alloy. *Acta Mater.* **2018**, *149*, 377−387.
(42) Lian, J.; Wang, L. M.; Sun, K.; Ewing, R. C. In Situ TEM of Radiation Effects in Complex Ceramics. *Microsc. Res. Technol.* **2009**, *72* (3), 165−181.
(43) Öhman, S.; Ek, G.; Nagy, G.; Törndahl, T.; Primetzhofer, D.; Boman, M. Circumventing Thermodynamic Constraints in Nucleation-Controlled Crystallization of Al2 TiO5 -Based Chemical Vapor Deposition Coatings. *Chem. Mater.* **2022**, *34* (11), 5151−5164.
(44) Öhman, S.; Forslund, A.; Lindblad, R.; Nagy, G.; Broqvist, P.; Berggren, E.; Johansson, F. O. L.; Törndahl, T.; Primetzhofer, D.; Boman, M. Role of Oxygen in Vacancy-Induced Phase Formation and Crystallization of Al 2 TiO 5 -Based Chemical Vapor-Deposited Coatings. *J. Phys. Chem. C* **2023**, *127* (13), 6456−6465.
(45) Dill, E. D.; Josey, A. A.; Folmer, J. C. W.; Hou, F.; Martin, J. D. Experimental Determination of the Crystallization Phase-Boundary Velocity in the Halozeotype CZX-1. *Chem. Mater.* **2013**, *25* (20), 3932−3940.
(46) Perepezko, J. H. Nucleation-Controlled Reactions and Metastable Structures. *Prog. Mater. Sci.* **2004**, *49* (3−4), 263−284.
(47) Hou, F.; Martin, J. D.; Dill, E. D.; Folmer, J. C. W.; Josey, A. A. Transition Zone Theory of Crystal Growth and Viscosity. *Chem. Mater.* **2015**, *27* (9), 115.
(48) Norberg, S. T.; Ishizawa, N.; Hoffmann, S.; Yoshimura, M. Redetermination of β-Al 2 TiO 5 Obtained by Melt Casting. *Acta Crystallogr. Sect. E Struct. Reports Online* **2005**, *61* (8), i160−i162.
(49) Hoffmann, S.; Norberg, S. T.; Yoshimura, M. Melt Synthesis of Al2TiO5 Containing Composites and Reinvestigation of the Phase Diagram Al2O3−TiO2 by Powder X-Ray Diffraction. *J. Electroceramics* **2006**, *16* (4), 327−330.
(50) Norberg, S. T.; Hoffmann, S.; Yoshimura, M.; Ishizawa, N. $Al_6Ti_2O_{13}$, a New Phase in the Al_2O_3−TiO_2 System. *Acta Crystallogr. Sect. C Cryst. Struct. Commun.* **2005**, *61* (3), i35−i38.
(51) Hoffmann, S.; Norberg, S. T.; Yoshimura, M. Structural Models for Intergrowth Structures in the Phase System Al2O3−TiO2. *J. Solid State Chem.* **2005**, *178* (9), 2897−2906.
(52) Ohya, Y.; Kawauchi, Y.; Ban, T. Cation Distribution of Pseudobrookite-Type Titanates and Their Phase Stability. *J. Ceram. Soc. Japan* **2017**, *125* (9), 695−700.
(53) Epicier, T.; Thomas, G.; Wohlfromm, H.; Moya, J. S. High Resolution Electron Microscopy Study of the Cationic Disorder in Al2TiO5. *J. Mater. Res.* **1991**, *6* (1), 138−145.

https://doi.org/10.1021/acs.cgd.3c00395
Cryst. Growth Des. 2023, 23, 7680−7687